KSME Journal, Vol. 7, No. 3, pp. 242~257, 1993

A Computational Study of Annular Cascade Flows Using a q-ω Turbulence Model with a Wall Function

D. S. Lee*

(Received February 7, 1993)

A computational code has been developed for steady viscous flows in three dimensional annular cascades. This code solves a special form of the thin-layer Navier-Stokes equations with a two-equation q-ω turbulence model in curvilinear coordinates using a time asymptotic method for steady state solutions. It employs a scalar implicit approximate factorization in time and a finite volume formulation with second-order upwind-differencing in space. A wall function treatment is implemented at solid boundaries for turbulence equations instead of integration to the wall to relieve gridding requirements. In order to validate the effectiveness of this code, computational studies have been made to access modeling capability for complex turbulent flow fields in three dimensional annular cascade geometries which typically include laminar-turbulent boundary layer transition. The results have been compared with both the computational studies with integration to the wall and the experimental studies. The wall function treatment was found to be reliable by predicting secondary flows and loss contours reasonably well.

Key Words: Cascade Flow, Turbine, Turbulence, Wall Function, Secondary Flow, Horseshoe Vortex, Passage Vortex, Pressure Loss

1. Introduction

Accurate numerical simulation of viscous flow characteristics has become increasingly important for the advanced turbomachinery. Turbine cascades are of particular concern because of complex flow phenomena. To be useful in the cascade design process, the method should be able to efficiently predict complex three-dimensional turbulent flow structures including aerodynamic losses, exit flow angle variation, and the highly nonuniform surface heat transfer. These are significantly influenced by strong secondary flow due to various types of vortices (horseshoe, passage and tip vortices) arising in cascade passages. Associated Reynolds numbers are usually moderate, so laminar-turbulent boundary layer transition is an essential part of this complex phenomenology.

In response to the need to improve predictive techniques, the author has been involved in a research effort to develop computational fluid dynamic codes for transonic cascade flows. In prior efforts by Knight and Choi(1987) and Lee and Knight(1989), efficiency and accuracy of the thin-layer approximated Navier-Stokes code based on a scalar implicit approximate factorization and a finite volume formulation were demonstrated for linear cascades including detailed comparison to experiments. A two-equation q-ω turbulence model suggested by Coakley(1983a) was found to give encouraging success in predicting laminar-turbulent boundary layer transition when turbulence model equations were integrated to the sublayer resolution down to $y^+ \sim 1$. This is

* Aeropropulsion Department, Korea Aerospace Research Institute, P.O.Box 15, Taeduok Science Town, Taejon 305-606, Korea

believed to be a key factor in predicting accurate heat transfer coefficients.

There is still a room for improvement of these codes in terms of practical use. The developed Navier-Stokes codes require a relatively large computer memory due to a fine grid structure needed to resolve turbulent boundary layers, about 50 Mbytes for typical three-dimensional simulations. Such a memory capacity is hardly available in mini-class computers which are getting popular in industry and research organizations. Consequently many are often forced to use coarse grid structures so that turbulent boundary layers are not properly resolved. Theoretical studies by Goldberg and Reshotko(1983) and Horstman(1984) and recent experimental results by Eibeck and Eaton(1985) also indicate there may be a logarithmic region in general. These facts motivated the study to assess wall function treatments for the q-ω turbulence model which could lead to significant reduction of gridding requirements for three-dimensional cascade flow computations. In a previous work by Kreatsoulas et al.(1988), the wall function treatment was used for the computation of a rectangular Stanitz elbow duct (Stanitz et al., 1953) and was found to give reliable results with secondary flows and loss contours essentially indistinguishable from those for integration to the wall.

This paper covers the extension of the wall function treatment to three-dimensional cascade flows. In this study, a wall function treatment was used to relieve gridding requirements, and integration to the wall using low turbulence Reynolds number modeling was also used when needed for comparison. A primary issue addressed in this study was a systematic evaluation of wall functions in the context of complex three-dimensional internal flow fields involving strong secondary flows. Rather than trying to prove the existence of a logarithmic region in general, the approach is to address the utility of such an assumption in situations representative of turbomachinery flow environments.

In Stanitz elbow case, boundary layers at the inlet region were all turbulent, so laminar-turbulent boundary layer transition was not a key consideration. That is no longer true in real cascade flows. However, boundary layer transition model was not incorporated in the present study only since no reliable one is yet one hands. Therefore, boundary layer at solid walls will be considered turbulent as often assumed in many other turbulence modelings. This will provide an opportunity to assess the importance of laminar-turbulent boundary layer transition in cascade flow fields and to make decision whether further study about a proper transition model will be useful in the future development.

The numerical formulation and modeling are first summarized before proceeding to preliminary code validation. The basic algorithm and wall function modeling are first assessed in a two-dimensional turbine cascade, which was experimentally studied by Langston et al.(1977). This includes comparison to results of integration to the wall approach and the experiment at midspan. The code is then applied to the three-dimensional viscous flows of a subsonic annular cascade of turbine vanes, studied experimentally by Goldman and Seasholtz(1982) and a transonic annular turbine stator studied, experimentally by Gardner(1979) on the Energy Efficient Engine (E^3) geometry. Computed results were compared with both results computed using integration to the wall method by Choi and Knight(1988) and the relevant experiments.

2. Analysis

2.1 Governing equations

The governing equations used in this study are the Reynolds averaged compressible three-dimensional Naiver-Stokes equation. The conservation law form of these equations can be written in a Cartesian coordinate system

$$\frac{\partial U}{\partial t}+\frac{\partial F}{\partial x}+\frac{\partial G}{\partial y}+\frac{\partial H}{\partial z}=0, \tag{1}$$

where

$$F=\begin{bmatrix} \rho u \\ \rho u^2+p-\tau_{11} \\ \rho uv-\tau_{21} \\ \rho uw-\tau_{31} \\ (E+p)u+q_1-\tau_{11}u-\tau_{12}v-\tau_{13}w \end{bmatrix}$$

$$G=\begin{bmatrix} \rho v \\ \rho u v-\tau_{12} \\ \rho v^2+p-\tau_{22} \\ \rho v w-\tau_{32} \\ (E+p)v+q_2-\tau_{21}u-\tau_{22}v-\tau_{23}w \end{bmatrix}$$

$$H=\begin{bmatrix} \rho w \\ \rho u w-\tau_{13} \\ \rho v w-\tau_{23} \\ \rho w^2+p-\tau_{33} \\ (E+p)w+q_3-\tau_{31}u-\tau_{32}v-\tau_{33}w \end{bmatrix} \quad (2)$$

The static pressure and total energy for a perfect gas are given as

$$p=\rho RT,$$
$$E=\frac{p}{\gamma-1}+\frac{\rho}{2}(u^2+v^2+w^2), \quad (3)$$

where γ is a ratio of specific heats.

The total stress tensor and heat flux vector which include both molecular and turbulent contributions by means of eddy viscosity hypothesis are represented by

$$\tau_{ij}=\mu\left(\frac{\partial u_i}{\partial x_j}+\frac{\partial u_j}{\partial x_i}\right)+\lambda\frac{\partial u_k}{\partial x_k}\delta_{ij},$$
$$q_i=-k\frac{\partial T}{\partial x_i},$$
$$\mu=\mu_L+\mu_T,$$
$$k=\frac{\mu_L}{Pr}+\frac{\mu_T}{Pr_T}, \quad (4)$$

where $(x_1, x_2, x_3)=(x, y, z)$, etc., and μ_L and μ_T are the molecular and turbulent (eddy) viscosities and thermal conductivity, k, is expressed in terms of the Prandtl numbers.

Molecular viscosity is related to the static temperature via Sutherland's law and eddy viscosity is obtained from the two-equation q-ω turbulence model. It is assumed that the second coefficient of viscosity, $\lambda=-\mu$ to simplify the viscous terms. This assumption is believed to cause little error since dilation effects are considered insignificant for transonic flows. Constant values are used for the Prandtl numbers.

The governing equations are transformed to boundary-conforming curvilinear coordinates. This is currently based on a sheared H-grid, with a careful control of transverse grid smoothness and specification of the normal distance of the first cell center off walls. By transforming only the independent variables (x, y, z) to the computational coordinates (ξ, η, ζ), the strong conservation law form can be maintained as

$$\frac{\partial U}{\partial t}+J\left(\frac{\partial \hat{F}}{\partial \xi}+\frac{\partial \hat{G}}{\partial \eta}+\frac{\partial \hat{H}}{\partial \zeta}\right)=0, \quad (5)$$

where

$$\hat{F}=(F\xi_x+G\xi_y+H\xi_z)/J,$$
$$\hat{G}=(F\eta_x+G\eta_y+H\eta_z)/J,$$
$$\hat{H}=(F\zeta_x+G\zeta_y+H\zeta_z)/J, \quad (6)$$

for a time-independent grid, where (ξ, η, ζ) are computational coordinates, and J is the determinant of the transformation Jacobian matrix computed by

$$J=\det\left[\frac{\partial(\xi, \eta, \zeta)}{\partial(x, y, z)}\right] \quad (7)$$

Recognize that Cartesian velocity components are retained as dependent variables. This required special care in constructing similarity transformations so that periodicity can be imposed properly, but it simplified evaluation of terms as well as conversion from earlier linear cascade codes. Viscous terms are incorporated via a special form of the thin-layer approximation which has been found to maintain accuracy on highly skewed grids, as noted in Knight and Choi(1987).

2.2 Turbulence model

Two-equation turbulence models seem to offer reasonable accuracy as well as ease of use in many turbulent flow calculations. In this study, Coakley's q-ω turbulence model (Coakley, 1983a) was chosen because of its numerical compatibility with the asymptotic time integration scheme. That is, timestep restrictions due to stiff turbulence source terms in the sublayer are minimal compared to other two-equation models. Particularly, prediction capability of heat transfer and laminar-turbulent transition phenomena has been very encouraging.

The dependent variables of this two-equation model are directly related to the turbulent kinetic energy, k, and dissipation rate, ε, via $q=k^{1/2}$ and $\omega=\varepsilon/k$; they define a turbulent velocity scale and inverse time scale, respectively. With these variables, eddy viscosity becomes

$$\mu_T=\rho C_\mu D q^2/\omega, \quad (8)$$

and near-wall damping function D for integration to the wall case is defined as

$$D=1-\exp(-\alpha\rho q d_n/\mu_L), \tag{9}$$

where $C_\mu=0.09$, and $\alpha=0.0065$, and d_n is defined using a Buleev length scale (Buleev, 1963) in terms of the normal distance to the nearest airfoil and endwall surfaces. In case of the wall function treatment, D becomes 1.0.

The conservation law form of transport equations for turbulent variables in the Cartesian tensor notation is given as

$$\frac{\partial}{\partial t}(\rho q)+\frac{\partial}{\partial x_i}(\rho u_i q)=\frac{\partial}{\partial x_i}\left[(\mu_L+\frac{\mu_T}{\mathrm{Pr}_q})\frac{\partial q}{\partial x_i}\right]+\frac{\rho q}{2}(C_\mu D\frac{\Theta}{\omega}-\omega),$$

$$\frac{\partial}{\partial t}(\rho\omega)+\frac{\partial}{\partial x_i}(\rho u_i\omega)=\frac{\partial}{\partial x_i}\left[(\mu_L+\frac{\mu_T}{\mathrm{Pr}_\omega})\frac{\partial\omega}{\partial x_i}\right]+\rho(C_1 C_\mu\Theta-C_2\omega^2) \tag{10}$$

where the strain rate invariant $\Theta=(u_{ij}+u_{ji})u_{ij}$. The flow dilation has been dropped in both turbulence source terms and Θ as negligible for transonic flows. Turbulent constants used are the same as in the original publication.

$$C_1=0.045+0.0405D \quad C_2=0.92$$
$$Pr_q=1.0 \quad Pr_\omega=1.3$$

In case of integration to the wall, making C_1 dependent on D is believed to be one reason that the q-ω model can be made relatively insensitive to timestep selection. Use of low turbulence Reynolds number terms also provides the possibility of rapid growth of q when $C_\mu D\Theta\geq\omega^2$. This enables to emulate the laminar-turbulent transition phenomenon as reported in many earlier studies. This capability is expected to be lost when the wall function treatment is used because $D=1$.

2.3 Wall function treatment

The basic purpose of a wall function treatment is to circumvent the need to resolve the viscous sublayer by assuming universality of the law-of-the-wall. This can considerably relieve near-wall gridding requirements, and also avoids stiffness due to turbulence source terms as well as highly refined mesh spacing. The classical form of law-of-the-wall is

$$\frac{u}{u_\tau}=\frac{1}{\chi}\ln\left(\frac{yu_\tau}{\nu}\right)+A, \tag{11}$$

where $u_\tau=(\tau_w/\rho)^{1/2}$ is a characteristic frictional velocity scale, $\chi=0.4$ is von Karman's constant, y measures distance normal to the wall, ν is the kinematic viscosity, and $A=5.5$ for a flat plate. This relation applies in the logarithmic region between the viscous sublayer (e. g., $y^+\cong yu_\tau/\nu>30$) and the law-of-the-wake region in the outer boundary layer for a wide variety of two-dimensional flows.

A variety of generalizations of Eq. (11) is to be found in the literature ; the most widely used one is

$$\frac{\rho uq}{\tau_w}=\frac{1}{\chi^*}\ln\left(\frac{qy}{\nu}E^*\right), \tag{12}$$

where q is a turbulent velocity scale as defined before. In the logarithmic region, it happens that $q\approx u_\tau C_\mu^{-1/4}$ where $C_\mu=0.09$ enters the eddy viscosity definition ; thus, $\chi^*\approx\chi C_\mu^{1/4}$ and $E^*\approx EC_\mu^{1/4}$ are to be expected, where $E=9.13$ is directly relatable to A in Eq. (11)

The primary reason for preferring Eq. (12) derives from its heat transfer counterpart :

$$\frac{\rho C_P(T_w-T)q}{Q_w}=\frac{1}{\chi_h}\ln\left(\frac{qy}{\nu}E_h\right), \tag{13}$$

where T is temperature, Q_w is the wall heat flux per unit area, and alternate constants χ_h and E_h are involved. In a separated flow, measurements indicate that the heat transfer rate is near its maximum at the reattachment point, a behavior that is at least qualitatively reproduced by this form (Launder, 1984). Howerver, the counterpart of Eq. (11) would predict no heat ransfer where the shear stress is zero. A secondary advantage of Eq. (12) is that iteration for u_τ and hence τ_w at each timestep is avoided.

Implementation details will be explained in two-dimensions, recognizing the grid structure involves a cell face at boundaries. Cell centers are denoted by integers in that follows, flux boundaries by integers plus 1/2, and the wall is at the cell face "3/2." Basic relationships are

$$\frac{\tau_w}{\rho} \simeq \left(\frac{\mu+\mu_T}{\rho}\right)_{3/2} \frac{u_2-u_1}{y_2-y_1} = \varkappa^* u_2 q_2 / \ln\left(\frac{q_2 y_2 E^*}{\nu_2}\right),$$
$$q_1 = q_2 - 2(q_3-q_2)\frac{y_{3/2}-y_2}{y_3-y_2},$$
$$\omega_1 = \omega_2\left(1+\frac{y_2-y_1}{y_{7/4}}\right), \qquad (14),$$

where all quantities at the flux boundary are evaluated by arithmetic averaging for consistency with the original coding, and the expression for ω represents asymptotic linear behavior in the logarithmic region. Recognize that above quantities below the wall (i. e., index=1) are fictitious physically and have meaning only in the sense that they assure proper transport at the first flux boundary.

Values of $\varkappa^*$ and E^* were chosen to give reasonably accurate predictions of skin-friction for a flat plate boundary layer with zero pressure gradient. This was accomplished by setting $\varkappa^* = \varkappa/\beta$, $E^* = E/\beta$, and optimizing β based on the skin-friction coefficient. Two-dimensional studies led to $\beta=2$, a value about 10 percent larger than $C_\mu^{-1/4}$ estimated from relations after Eq. (12). That value was not adjusted for the three-dimensional studies, nor was any other turbulence constant.

A basic issue in extending wall function treatments to three-dimensional cases is when flow turning ceases as the boundary is approached, because application of Eqs. (11) or (12) implicitly assumes fixed flow angle. Theoretical work by Goldberg and Reshotko(1983) indicates that there generally is a logarithmic region, with flow turning beginning for $y^+ > 40 \sim 70$ and primarily occurring in the defect layer. The treatment in the present study assumes the limiting flow angle is achieved well outside the sublayer and is fixed for much smaller values of y^+ in applying Eq. (12). Note that restrictions on y^+ at the first flux boundary arise in order for this to be assured. These are generally more stringent than for two-dimensional flows, and in consequence the gains for complex three-dimensional flow fields may not be as large. For three-dimensional cases, "y" is again treated as a Buleev-type variable measuring distance to walls.

2.4 Numerical method

The steady solution to the governing equations is obtained using the asymptotic time integration scheme based on a scalar implicit approximate factorization algorithm. This involves iterative application of a linear operator of the form:

$$L(\delta t,\ U)\cdot \delta U = \Delta U, \qquad (15)$$

where δU is the change in solution over timestep δt, $\Delta U = -R^n\,\delta t$ represents the degree of unsteadiness, and R^n is the residual vector evaluated from steady flow terms at time level n. Finite volume formulation is employed with flux boundaries coinciding with walls.

Residual is evaluated explicitly based on second-order upwind-differencing scheme suggested by Coakley(1983b). Advantages of this method over central-differencing plus damping are the substantial improvements in speed and accuracy. The dissipation function for this scheme is evaluated based on nonconservative variables and characteristic increments. This can be illustrated by considering the discretization of F in ξ direction.

$$\frac{\partial \hat{F}}{\partial \xi} \rightarrow \frac{1}{\delta\xi}(\hat{F}^*_{i+1/2} - \hat{F}^*_{i-1/2}), \qquad (16)$$

where $\delta\xi = 1$, and the asterisks denote addition of numerical damping to assure near monotone behavior.

$$\hat{F}^*_{i+1/2} = \frac{1}{2}(\hat{F}_i + \hat{F}_{i+1} - D_{i+1/2}) \qquad (17)$$

Similarity transformations arising from characteristics theory are used in evaluating the dissipation function D

$$D_{i+1/2} = \delta f^+_{i+1/2} + \delta f^-_{i+1/2} - \delta f^-_{i-1/2} + \delta f^-_{i+3/2},$$
$$\delta f^\pm_{i+1/2} = \frac{1}{2} S^{-1}_{i+1/2}(|\Lambda_{i+1/2}| \pm \Lambda_{i+1/2}) \cdot S_{i+1/2}(U_{i+1} - U_i), \qquad (18)$$

where S is a matrix of left eigenvectors associated with ξ direction, Λ is a diagonal matrix of corresponding eigenvalues, and δf defines characteristic increments. Elements of S and Λ are evaluated at the cell face using Roe's averaging (Roe, 1981).

For the implicit update procedure, the scalar form of the approximate factorization algorithm is employed. Using the similarity transformation

by characteristic theory, transformed inviscid flux Jacobian matrices

$$A=\frac{\partial \hat{F}}{\partial U},\ B=\frac{\partial \hat{G}}{\partial U},\ C=\frac{\partial \hat{H}}{\partial U}, \tag{19}$$

can be diagonalized as

$$\begin{aligned} A&=S_\xi^{-1}\Lambda_\xi S_\xi,\\ B&=S_\eta^{-1}\Lambda_\eta S_\eta,\\ C&=S_\zeta^{-1}\Lambda_\zeta S_\zeta, \end{aligned} \tag{20}$$

where S and Λ are defined as before.

Since the Jacobians for viscous terms cannot be diagonalized, viscous terms are treated approximately by adding a second derivative times the maximum eigenvalue of the viscous Jacobian for each of the transverse direction. This results in a following differential form

$$\begin{aligned} &(I+J\delta t\frac{\partial}{\partial \xi}\Lambda_\xi)\cdot S_\xi\delta U^*=S_\xi\Delta U,\\ &(I+J\delta t\frac{\partial}{\partial \eta}\Lambda_\eta+I\delta t\nu_\eta\frac{\partial^2}{\partial \eta^2})\cdot S_\eta\delta U^{**}\\ &\quad=S_\eta\delta U^*\\ &(I+J\delta t\frac{\partial}{\partial \zeta}\Lambda_\zeta+I\delta t\nu_\zeta\frac{\partial^2}{\partial \zeta^2})\cdot S_\zeta\delta U=S_\zeta\delta U^{**} \end{aligned} \tag{21}$$

Sine the coefficient matrices, Λ and ν, are diagonal with respect to characteristic increments, solutions to Eq. (21) require a sequence of linear transformations and scalar algebraic relations, which implies much fewer calculation than for a block implicit scheme.

First-order upwinding was used for the discretization of inviscid terms and central differencing was used for viscous contributions. This leads to scalar tridiagonal systems and provides acceptable convergence. Accuracy of the final steady solution is, of course, not affected by this choice of differencing scheme for the implicit part.

A similar treatment of turbulent source terms through the implicit coefficient matrix originally suggested by Coakley(1983a) was found less than promising in the present code structure. This was replaced by a suitable scalar approximation to the Jacobian of the turbulence source terms, which was incorporated in a post-processing step to make it perform better for a sudden start calculation.

The boundary conditions are treated fully implicitly in order to maintain the high convergence rate of the overall implicit method. Extraneous boundary conditions also arise with second-order accurate differencing scheme, such as determination of the static pressure at solid walls. The approach used for this kind of boundary conditions is to employ a first-order accurate treatment for implicit update procedure, and then correct results explicitly to satisfy full second-order accuracy. This essentially eliminates timestep restrictions associated with boundary conditions and maintains simplictity.

In order to accelerate convergence, dual timestep selection criteria are also used to determine local timesteps which spatially vary. With CFL $\sim$3 in the inviscid core and much larger CFL in viscous-dominated regions, comparable convergence rates in coarse and refined grid regions were achieved. Details of boundary condition treatments and dual timestep selection scheme was described in Knight and Choi(1987).

3. Results and Discussions

Three sets of test cases were computed to assess performance of the present analysis method. The first one is for a large scale Langston linear cascade (Langston et al., 1977). Others are annular cascades ; one is for a NASA subsonic annular vane studied experimentally by Goldman and Seasholtz(1982), and the orther is for the NASA Energy Efficient Engine(E^3) annular vane with an S-shaped tip-side endwall investigated by Gardner(1979).

3.1 Langston cascade

A two-dimensional version of the present method was first developed and validated by considering the large scale Langston linear cascade. A case considered in the present study is the cascade set at an inlet angle of 44.6°. The upstream inlet Mach number was 0.1 and the exit Mach number was about 0.16. The corresponding Reynolds numbers based on axial chord length were 5.5×10^5 and 1.0×10^6, respectively. Measured inlet free stream turbulence quantities are not available, so free stream turbulence intensity was assumed to be 3%.

Integration to the wall calculations were done for the midspan profile on a simple sheared H-grid with 81×42 points in ξ and η direction, respectively. The minimum axial grid spacing near the leading edge and trailing edge was 0.005 C_x, and the maximum axial grid spacing was 0.05 C_x, where C_x is the axial chord length. Near the blunt trailing edge, the grid spacing on the blade surface was determined by using 10° angular increments to adequately describe its circular shape there. The normal distance of the first grid point from the blade surface was chosen as $1 \times 10^{-4} C_x$ to ensure sublayer resolution down to $y^+ \sim 1$. The wall function treatment calculation employs 36 grid points in η direction with minimum spacing of $1 \times 10^{-3} C_x$. With this minimum grid spacing, the center of the first cell off the wall locates sufficiently away from the viscous sublayer in most region. The further reduction of number of grid points in η direction can be easily anticipated, but was not accomplished only due to the failure of grid generation algorithm.

Figures 1 and 2 compared the contours of the static pressure coefficient and Mach number at the midspan, respectively, where the static pressure coefficient was defined based on the upstream dynamic head. Note that the contour patterns in computational results are essentially unaffected by the wall function treatment. Measurement data were not available for comparison. Figure 3 shows the axial distribution of the static pressure coefficient at blade surfaces. As expected from Fig. 1, excellent agreement between com-

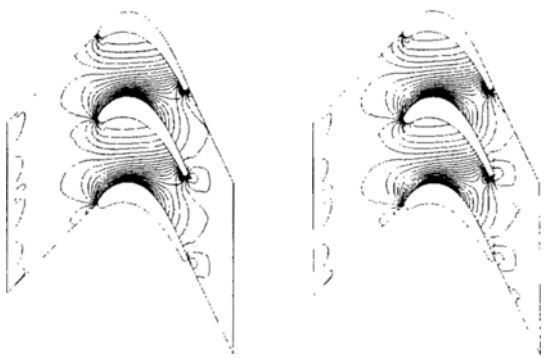

Fig. 1 Midspan static pressure coefficient contours for the Langston linear cascade

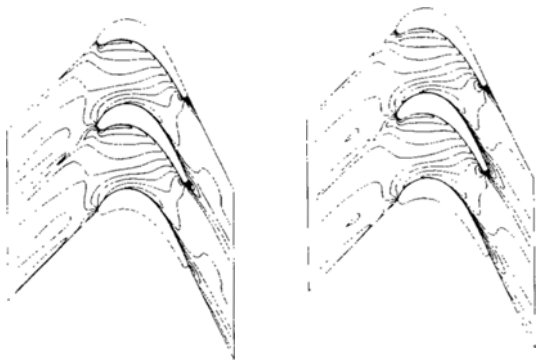

Fig. 2 Midspan Mach number contours for the Langston linear cascade

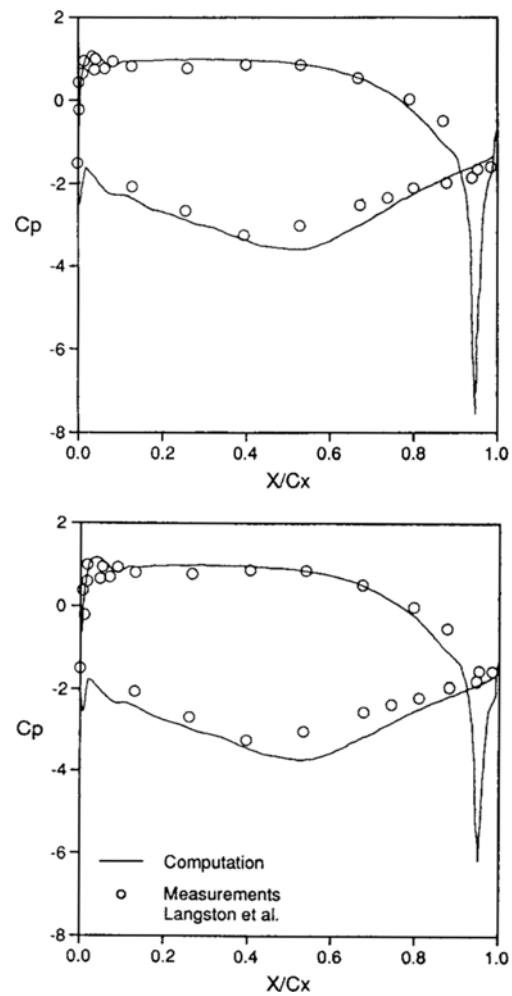

Fig. 3 Static pressure distributions on midspan blade surface for the Langston linear cascade

putational results was achieved. Both solutions, however, show slight disagreement at the suction surface after the choke point with the experiment. Sharp peaks at the pressure surface were due to the separation at the rounded trailing edge, which was not measured in the experiment.

Axial variations of the skin-friction coefficient at the suction surface are compared in Fig. 4. There are notable discrepancies between two solutions. The result obtained by integration to the wall method shows rapid decrease of skin-friction near the mid-chord region while the wall function treatment produced smooth decrease over the entire suction surface. This is due to the lack of laminar-turbulent boundary layer transition mechanism of the wall function treatment.

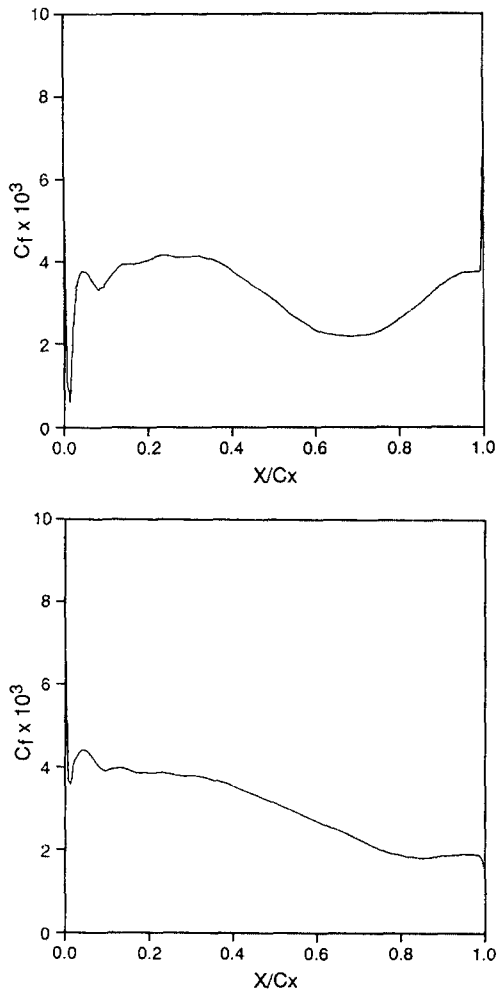

Fig. 4 Axial variation of skin-friction coefficient on the suction surface of the Langston linear cascade

This can be seen more evidently in Fig. 5 showing U^+ versus ln (Y^+) velocity profiles in boundary layer at several axial locations. In these figures, circles represent the computed values of U^+ and ln(Y^+) at each grid cell and solid lines indicate the typical law-of-the-wall for the flat plate, $U^+=2.44 \ln (Y^+)+5.0$. Close observation of results computed by integration to the wall shows that a transition from laminar to turbulent happens at $x=0.05\ C_x$, relaminarization occurs near $x=0.5\ C_x$, and flow goes through the second laminar-to-turbuleut transition near $x=0.9\ C_x$ at the suction surface. Here x measures from the leading edge. On the other hand, velocity profiles at the suction surface boundary layer computed by the wall function treatment are turbulent everywhere as expected.

Relaminarization predicted with integration to the wall method deserves further study though. In a previous study (Lee and Knight, 1989), relaminarization did not occur with O−H grid formulation, which is believed to produce better prediction especially in the boundary layer region. Based on the present results, the wall function treatment performs reasonably well in terms of predicting the pressure distribution in the cascade passage despite lack of capability predicting boundary layer transition at least in two-dimensional flow analysis. This could, however, mean that the transitional effect is insignificant in determining pressure distribution.

3.2 Subsonic NASA stator

The code was later extended to the three-dimensional subsonic annular stator cascade studied experimentally at NASA Lewis. The detailed cascade geometry and experimental configuration can be found in Goldman(1982). Mean values of exit Mach number was about 0.8 and 0.7 at the hub and tip, respectively. The untwisted vanes, of constant profile from hub to tip, had a height of 38.10 mm and an axial chord of 38.23 mm. The stacking axis of the vane was located at the center of the trailing edge circle. The vane aspect ratio and the solidity at the mean radius based on the axial chord were 1.0 and 0.93, respectively. The

stator hub-tip radius ratio was 0.85 and the tip diameter was 508 mm.

In the present calculation with the wall function treatment, many meshes with different minimum grid spacings were tried to ensure that the first grid points locate in the logarithmic region in most boundary layer. The best solution among tried ones was obtained with a total number of 98, 112 computational grid points ($73 \times 32 \times 42$; they are numbers of grid points in the axial, circumfer-

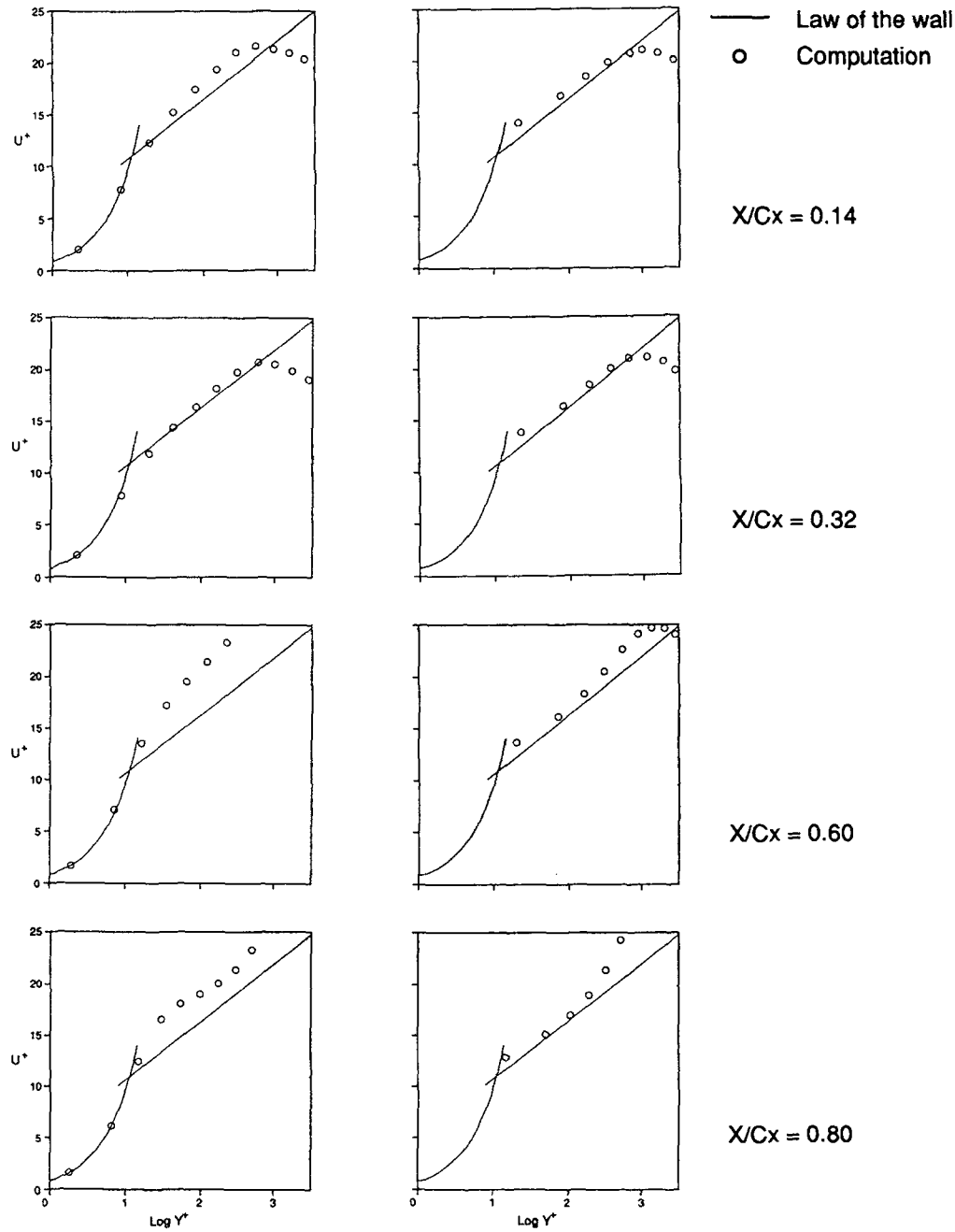

Fig. 5 Comparison of $U^+ - Y^+$ velocity profiles at the suction surface of the Langston linear cascade

ential, and radial directions, respectively.) A minimum grid spacing in the circumferential direction is $2.5\times10^{-3}\,C_x$, and the maximum grid spacing is about 5 percent of circumferential pitch at each radial position. In the radial direction, the minimum grid spacing of $2.5\times10^{-3}\,C_x$ is used at both hub and tip surfaces, and the maximum grid spacing is also 5 percent of the span distance. In the original study with integration to the wall by Choi and Knight(1988), a total number of grid points was 171,696($73\times42\times56$) with minimum grid spacings were $1\times10^{-4}\,C_x$ in both the circumferential and radial directions. Therefore, the gain due to grid saving is 1.75 with the wall function treatment. Converged results were achieved much faster than the integration to the wall approach with 500 timesteps.

Figure 6 shows the axial distribution of the static pressure on blade surfaces for three representative spanwise locations. As shown in these figures, computational results are indistinguishable and they compare very well with the corresponding measurements except only at the suction surface near the hub. The spanwise distributions of the static pressure mass-averaged across the pitch are also compared in Fig. 7. They show outstanding agreement, too. These results are surely expected because pressure variations on blade surfaces are mainly inviscid phenomena. Accuracy of the wall function treatment can be found in the loss prediction and the flow angle variation at exit plane, which are mainly due to viscous effects of the flows.

Figure 8 shows the flow angle variation versus the radial direction at after-mixed flow conditions. The predicted values are taken at about 29 percent of the chord length downstream from the trailing edge, and the experimental data was measured at 33 percent chord downstream. This difference due to a grid structure is almost negli-

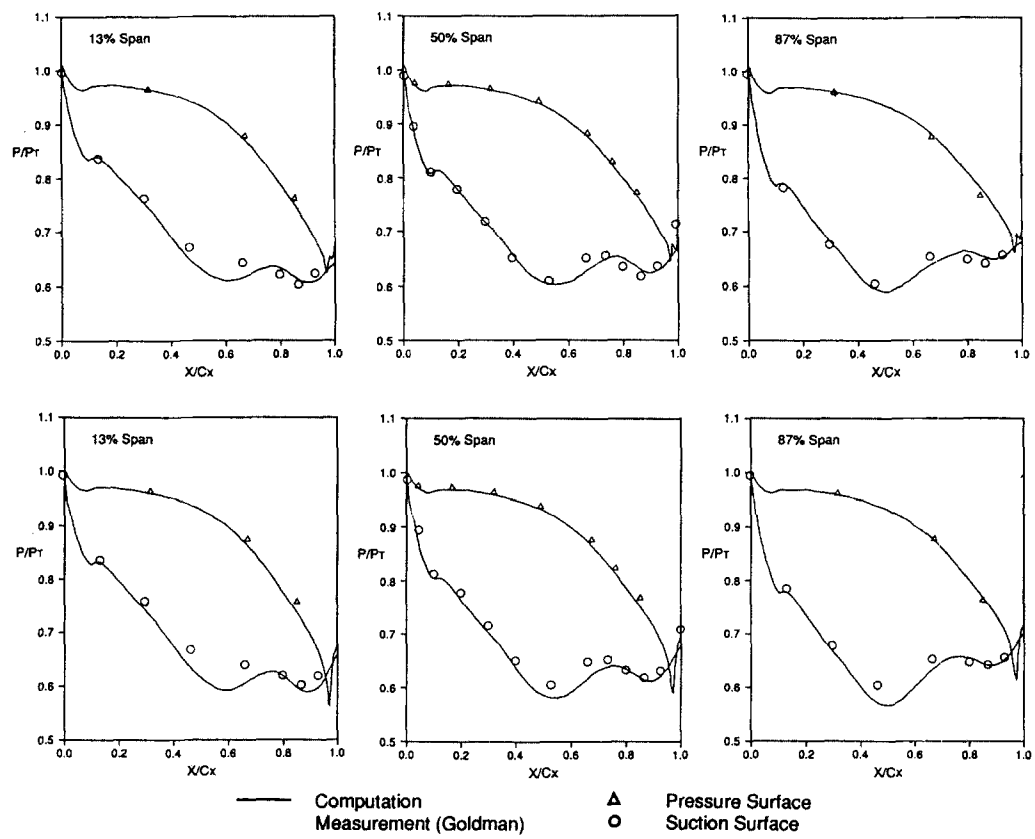

Fig. 6 Static pressure distributions on blade surfaces for the NASA subsonic vane

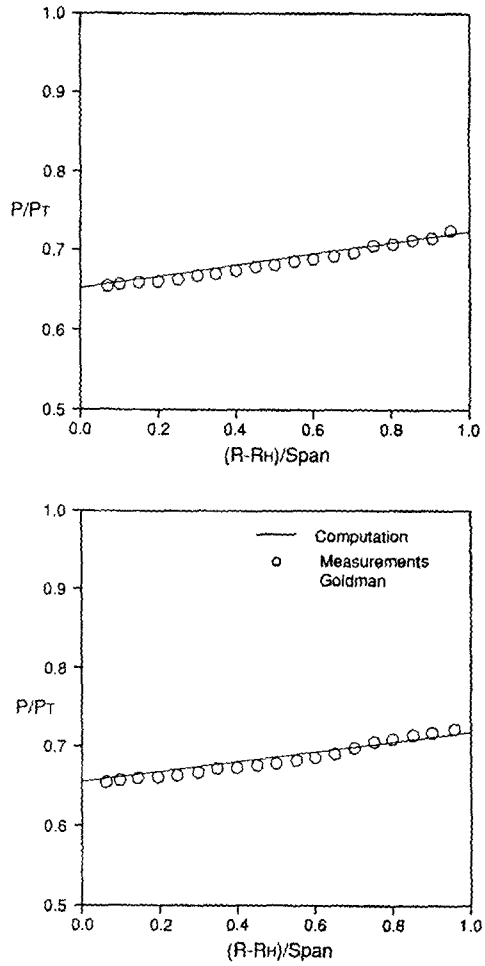

Fig. 7 Spanwise variation of mass-averaged static pressure at $X = 1.33\ C_x$ for the NASA subsonic vane

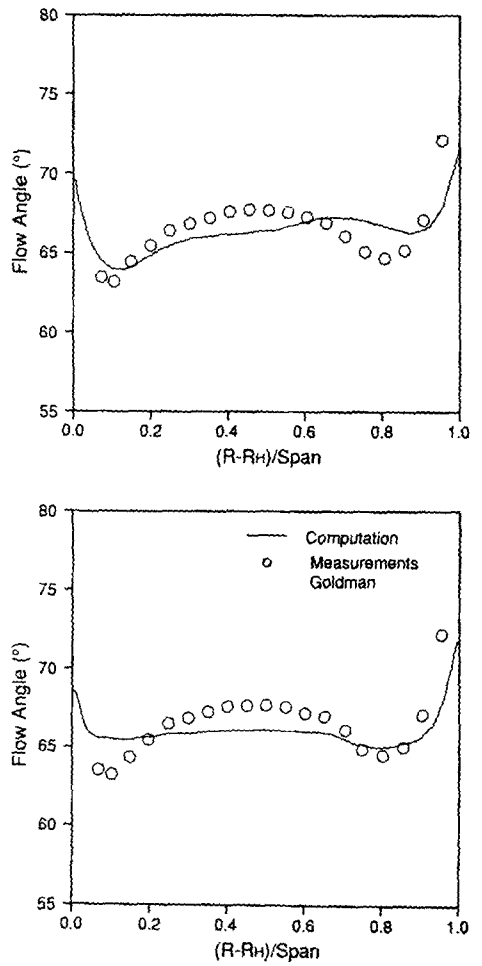

Fig. 8 Spanwise variation of after-mixed exit flow angle at $X = 1.33\ C_x$ for the NASA subsonic vane

gible. These are averaged based on mass flux along the circumferential direction at a given radial location. The wall function treatment predicts much flatter variation of exit angle in the core part of the span compared to both the result computed by integration to the wall and the measurement, although predicted values are still within the accuracy of the measurement, $\pm 1.2°$. This implies that the strength of the secondary flow at endwalls is predicted much weaker than it should be. Such underprediction is more evident at the hub region than the tip region.

The same observation can be made in the comparison of the mass-averaged total pressure loss predictions at the same exit location shown in Fig. 9. These total pressure loss predictions agree very well with the experiment except at about 15 percent of the span near the hub. The wall function treatment underpredicted the loss while integration to the wall overestimated it in that region. This indicates that both formulation did not accurately handle passage vortex development.

The vane efficiency contours based on kinetic energy are compared in Fig. 10. Note that the passage vortex locations near the tip are well predicted by the wall function treatment when compared to the measure-
shown

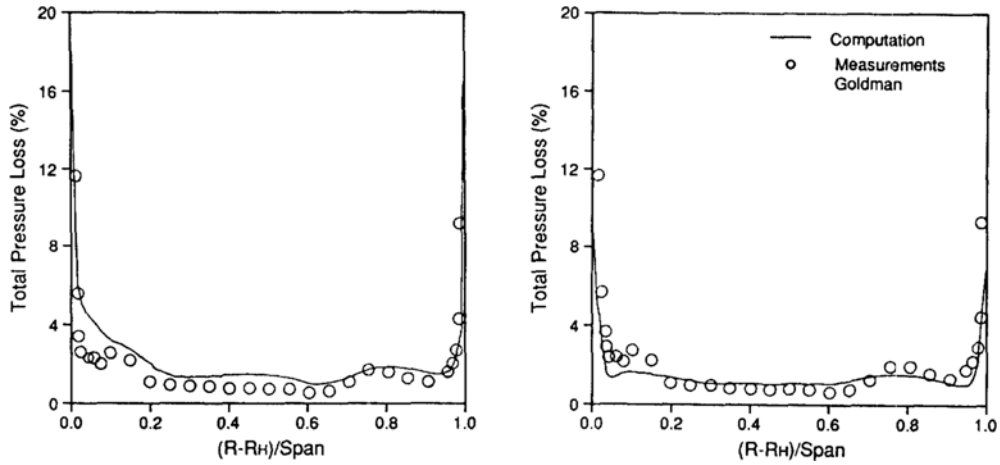

Fig. 9 Spanwise variation of mass-averaged total pressure loss at X=1.33 C_x for the NASA subsonic vane

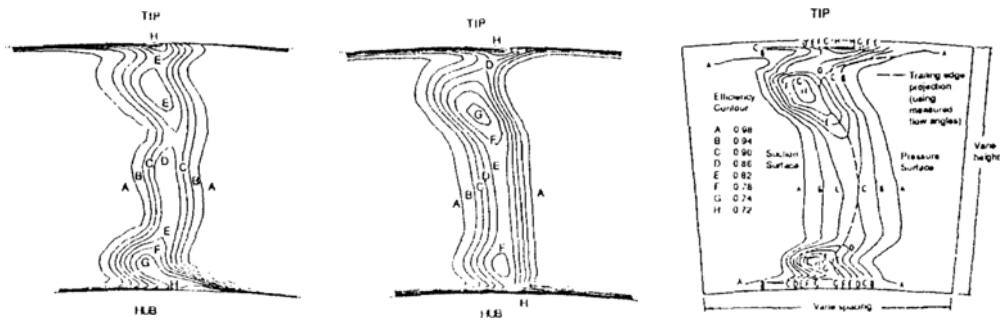

Fig. 10 Efficiency contours at X=1.33 C_x for the NASA subsonic vane

On the other hand, integration to the wall shows excellent agreement with the experiment. This required further study about the detailed information on turbulent quantities and passage vortex, which will be reported in the future.

3.3 Transonic NASA EEE vane

Evaluation of the wall function was performed for the transonic flow through a twisted annular vane in a single-stage with 0.35 reaction, which is one of the energy efficient uncooled rig tested by Gardner(1979). Mach number at the after-mixed condition is about 1.01, the Reynolds number based on exit free stream condition and vane axial chord length is about 1.3×10^6 and the design exit flow angle is 10.4°.

For the wall function treatment, a mesh of 74, 752 grid points ($73\times32\times32$) was generated using simple algebraic relationships. In the original study using integration to the wall approach by Choi and Knight(1988), a mesh of $73\times42\times42$ (=128, 772) grid points was used for this case. The factor of grid saving with these meshes is 1. 72. This factor should not be regarded small since the original grid was considered rather coarse to have a good resolution of the turbulent boundary layer. Minimum and maximum grid spacing are $1\times10^{-3}\,C_x$ and 0.05 C_x, respectively, in both circumferential and radial directions. In the original grid, minimum and maximum spacings were $2.1\times10^{-4}\,C_x$ and 0.105 C_x in the circumferential direction, and they were 1.7×10^{-4} C_x and 0.085 C_x in the radial direction, respectively.

Figure 11 shows the axial distribution of the static pressure profiles on the vane surface for three spanwise locations. As in the subsonic case, both computational results show no discernible

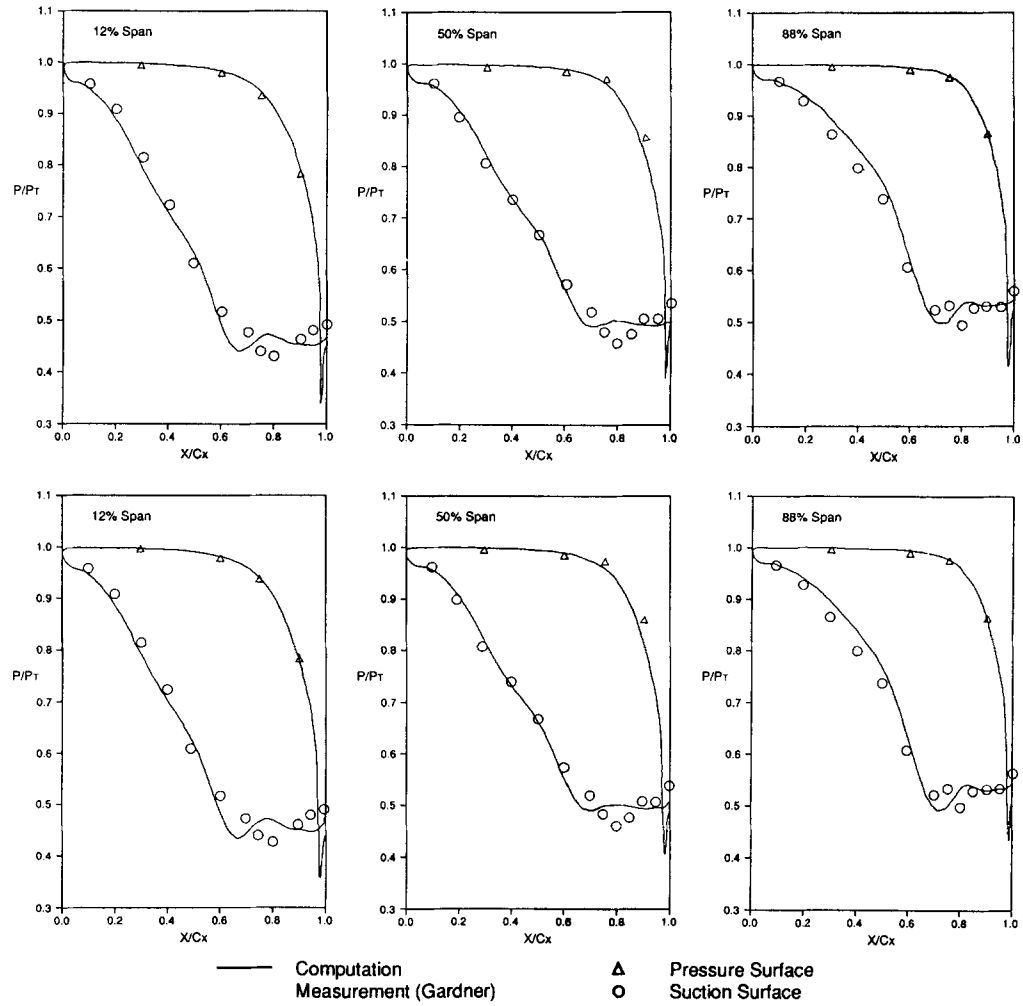

Fig. 11 Static pressure distributions on blade surfaces for the transonic NASA E^3 vane

difference and compare well with the measurements. These solutions, however, show minor defects near the suction surface trailing edge. In Fig. 12, area-averaged exit Mach number profiles at 1.4 C_x downstream from the trailing edge are compared with measurements. The precise axial location of measurements was not available. Although computed solutions show good agreement, they do not match the measured data well in 20% of the span near the hub. Both solutions show much thinner boundary layer thickness at the hub side. The previous study mentioned the inability to match unknown detailed inflow conditions including free-stream turbulence quantities and incoming boundary layers as a possible cause of this discrepancy. This issue could not be resolved in this study.

Distributions of computed exit flow angle, shown in Fig. 13, again compare rather poorly with measurements in the hub side half. Figure 14 compares the spanwise variation of total pressure loss at an exit plane, defined at each radial location by area-averaging along the circumferential direction. It is surprising to see that loss values predicted by the wall function treatment are almost twice higher than the measured values at the core region while it severely underpredicts the flow turning near the hub. Figure 15 shows the

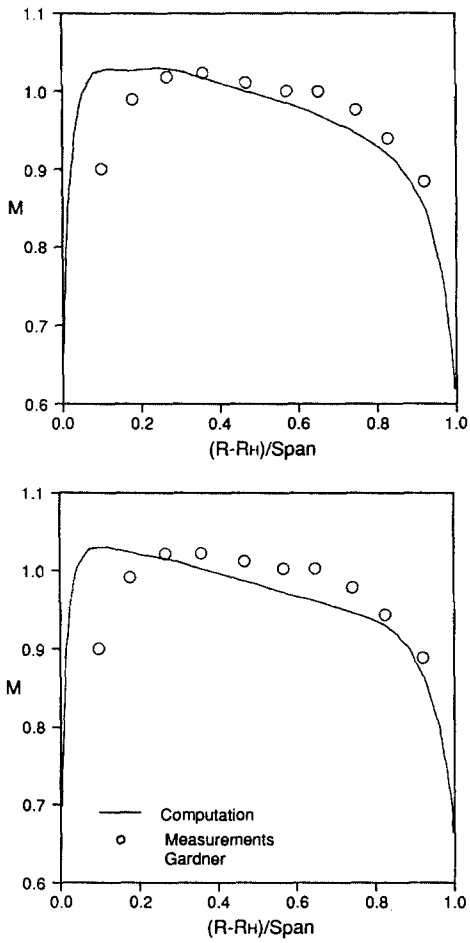

Fig. 12 Spanwise variation of area-averaged exit Mach number at $X=1.4\ C_x$ for the transonic NASA E^3 vane

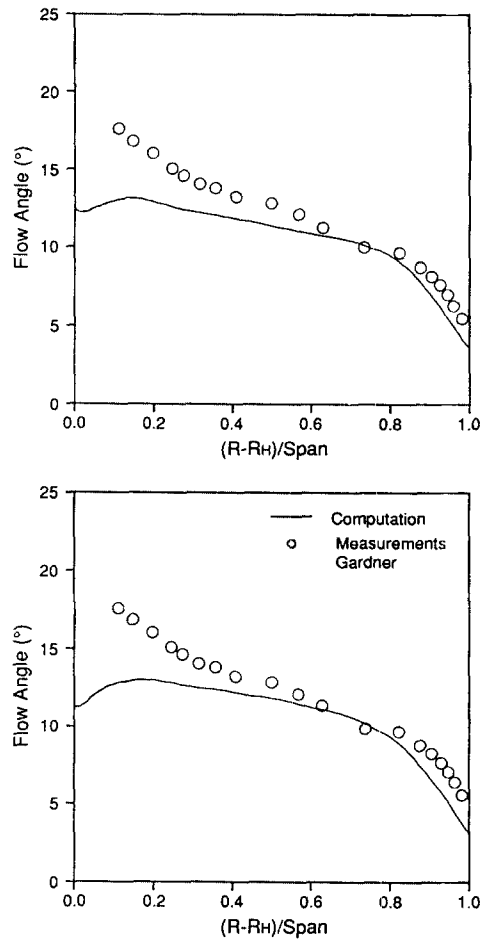

Fig. 13 Spanwise variation of area-averaged exit flow angle at $X=1.4\ C_x$ for the transonic NASA E^3 vane

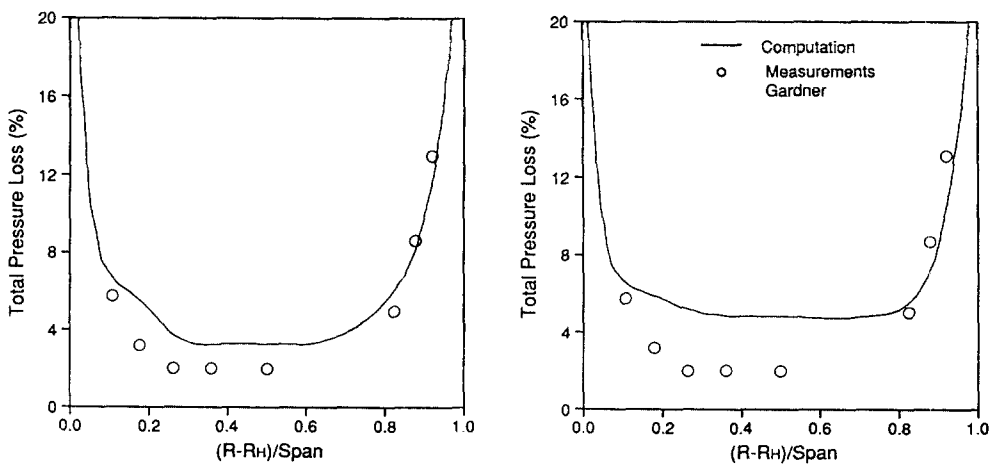

Fig. 14 Spanwise variation of area-averaged total pressure loss at $X=1.4\ C_x$ for the transonic NASE E^3 vane

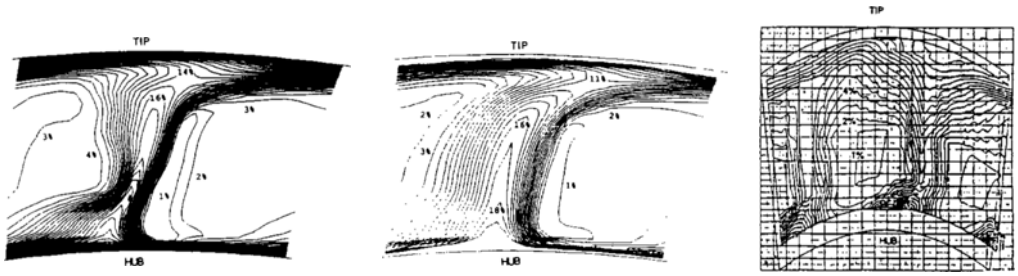

Fig. 15 Total pressure loss contours at $X=1.4\,C_x$ for the transonic NASA E^3 vane

total pressure loss contours at the exit plane. As in the subsonic vane case, predictions at the hub side by the wall function treatment are in poor agreement with measurements while those computed by integration to the wall show reasonably good formation.

In general, the current wall function treatment failed to predict correct development of the secondary flow formation, especially near the hub region. This is somewhat disappointing since the similar treatment show promising features in earlier Stanitz elbow calculation by Kreatsoulas et al.(1988). In three-dimensional cascade flows such as ones computed in this study, horseshoe vortices as well as passage vortices have significant effects in the development of the secondary flow, while passage vortices is the only dominant secondary flow mechanism in the duct flow. Consequently, the present wall function can be said to be insufficient to capture the precise development of the horseshoe vortex in cascade flows. This is believed to be due to eddy viscosity computed too high in core region compared to integraion to the wall results, as also observed in the Stanitz elbow calculation. Absence of an intermittency factor in the current two-equation model can be a primary reason for such high eddy viscosity production. Inclusion of streamline curvature effects notable in the swirl flow can be a possible remedy. Effects of transitional phenomena on the development of the passage vortex should be also investigated.

4. Conclusion

A wall function treatment was developed for the two-equation q-ω model and was tested in annular cascade geometries. Based on a detailed computational study comparing it with integration to the wall and experiments, the wall function treatment was found to perform reasonably well in predicting general characteristics of cascade flows. Improved computational economy was provided with reduction of grid points. Also, convergency rate is considerably enhanced compared to integration to the wall.

The capability to describe accurate formation of strong secondary flows, however, does not meet the expectation. To predict correct development of horseshoe vortices in cascade flows, inclusion of an intermittency factor and stream curvature effect associated with swirl flows should be carefully considered to curtail the high eddy viscosity predicted by the wall function treatment in the core region. More complete validation of the wall function treatment must include the evaluation of heat transfer prediction and appropriate boundary layer transitional models.

Acknowledgment

This research was conducted under the sponsorship of Textron Lycoming's Research and Development Program. I wish to thank the management of Textron Lycoming and Korea Aerospace Research Institute for their support and permission to present these results.

References

Buleev, N., 1963, "Theoretical Model of the Mechanism of Turbulent Exchange in Fluid

Flows," Atomic Energy Research Establishment, Hartwell, England, AERE Translation 957.

Choi, D. and Knight, C.J., 1988, "Computation of 3D Viscous Annular Cascade Flows," AIAA-88-3092, AIAA/ASME/ASEE 24th Joint Propulsion Conference.

Coakley, T.J., 1983a, "Turbulence Modeling Methods for the Compressible Navier-Stokes Equations," AIAA-83-1693, 16th Fluid and Plasmadynamics Conference.

Coakley, T.J., 1983b, "Implicit Upwind Methods for the Compressible Navier-Stokes Equations," AIAA-83-1958, 6th Computational Fluid Dynamics Conference.

Eibeck, P.A. and Eaton, J.K., 1985, "An Experimental Investigation of the Heat Transfer Effects of a Longitudinal Vortex Embedded in a Turbulent Boundary Layer," Report MD-48, Thermo. Division, Dept. of Mechanical Engineering, Stanford University.

Gardner, W.B., 1979, "Energy Efficient Engine, High-Pressure Turbine Uncooled Rig Technology Report," NASA CR-165149.

Goldberg, U. and Reshotko, E., 1983, "Scaling and Modeling of Three-Dimensional, Pressure-Driven Turbulent Boundary Layers," AIAA-83-1695, 16th Fluid and Plasma Dynamics Conference.

Goldman, L.J. and Seasholtz, R.G., 1982, "Laser Anemometer Measurements in an Annular Cascade of Core Turbine Vanes and Comparison with Theory," NASA Technical Paper 2018.

Horstman, C.C., 1984, "A Computational Study of Complex Three-Dimensional Compressible Turbulent Flowfields," AIAA-84-1556, 17th Fluid Dynamics, Plasma Dynamics, and Lasers Conference.

Knight, C.J. and Choi, D., 1987, "Development of a Viscous Cascade Code Based on Scalar Implicit Factorization," AIAA-87-2150, AIAA/SAE/ASME/ASEE 23rd Joint Propulsion Conference.

Kreatsoulas, J.C., Lee, D., Ballantyne, A. and Knight, C.J., 1988, "Experimental/Computational Study of Viscous Flow in a Contracting Rectangular Elbow," AIAA Journal, Vol. 26, pp. 1434~1441.

Langston, L.S., Nice, M.L. and Hooper, R.M., 1977, "Three-Dimensional Flow Within a Turbine Cascade Passage," ASME J. of Engineering for Power, Vol. 99, pp. 21~28.

Launder, B.E., 1984, "Second-Moment Closure : Methodology and Practice," Turbulence Models and Their Applications, Vol. 2, Editions Eyrollers, Paris, France.

Lee, D. and Knight, C.J., 1989, "Evaluation of an O-H Grid Formulation for Viscous Cascade Flows," AIAA-89-0207, 27th Aerospace Sciences Meeting.

Roe, P.L., 1981, "Approximate Riemann Solvers, Parameter Vectors, and Difference Schemes," J. of Computational Physics, Vol. 43, pp. 357~372.

Stanitz, J.D., Osborn, W.M. and Mizisin, S., 1953, "An Experimental Investigation of Secondary Flow in an Accelerating, Rectangular Elbow with 90° of Turning," NACA 3015.